

Research



Cite this article: Liu KT, Paulino GH. 2024

Geometric mechanics of hybrid origami assemblies combining developable and non-developable patterns. *Proc. R. Soc. A* **480**: 20230716.

<https://doi.org/10.1098/rspa.2023.0716>

Received: 27 September 2023

Accepted: 15 December 2023

Subject Areas:

geometry, mechanics

Keywords:

tessellations, Poisson's ratio, auxetic behaviour, origami metamaterials

Author for correspondence:

G. H. Paulino

e-mail: gpaulino@princeton.edu

Electronic supplementary material is available online at <https://doi.org/10.6084/m9.figshare.c.7021226>.

Geometric mechanics of hybrid origami assemblies combining developable and non-developable patterns

Kevin T. Liu¹ and G. H. Paulino^{1,2}

¹Department of Civil and Environmental Engineering, and

²Princeton Materials Institute (PMI), Princeton University, Princeton, NJ 08544, USA

KTL, 0009-0009-3661-1261; GHP, 0000-0002-3493-6857

Origami provides a method to transform a flat surface into complex three-dimensional geometries, which has applications in deployable structures, metamaterials, robotics and beyond. The Miura-ori and the eggbox are two fundamental planar origami patterns. Both patterns have been studied closely, and have become the basis for many engineering applications and derivative origami patterns. Here, we study the hybrid structure formed by combining unit cells of the Miura-ori and eggbox patterns. We find the compatibility constraints required to form the hybrid structure and derive properties of its kinematics such as self-locking and Poisson's ratio. We then compare the aforementioned properties of the Miura-eggbox hybrid with those of the morph pattern, another generalization of the Miura-ori and eggbox patterns. In addition, we study the structure formed by combining all three unit cells of the Miura-ori, eggbox and morph. Our results show that such patterns have tunable self-locking states and Poisson's ratio beyond their constituent components. Hybrid patterns formed by combining different origami patterns are an avenue to derive more functionality from simple constituents for engineering applications.

1. Introduction

In recent years, the ancient art of origami has been used for engineering applications. Origami is a method to transform a flat surface into complex three-dimensional geometries and can provide advantages such as deployability, scalability, reconfigurability, tunability and manufacturability [1]. Origami-based

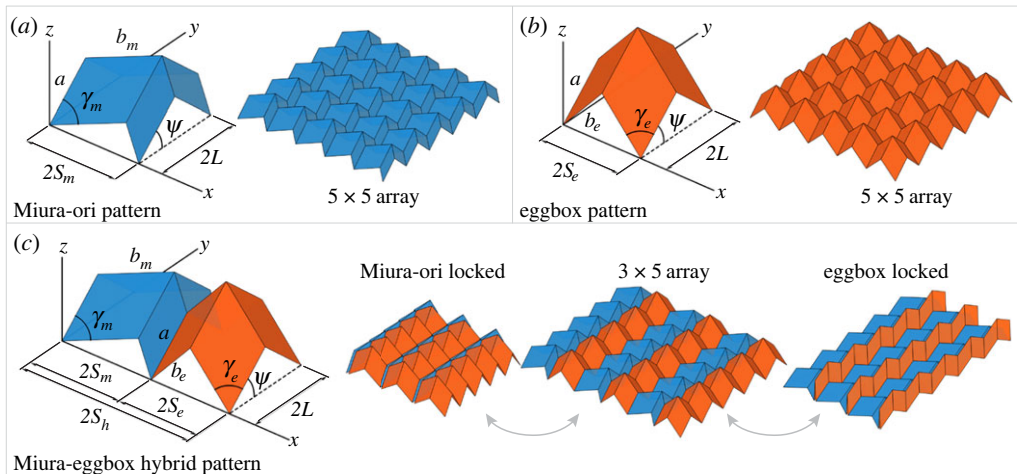


Figure 1. Geometry and notation of (a) standard Miura-ori with intrinsic parameters (a, b_m, γ_m), (b) standard eggbox with intrinsic parameters (a, b_e, γ_e) and (c) Miura-eggbox hybrid patterns. We display a unit cell and arrays formed for each pattern. The second row displays three configurations of a hybrid array, including the two limits of the configuration space where the Miura-ori and eggbox cells are flat-folded, respectively.

designs can be found in fields including deployable structures [2], materials science [3] and robotics [4]. The field is ubiquitous and thus the reader is referred to review papers such as [1,5].

The Miura-ori and eggbox are two fundamental planar origami patterns consisting of tessellated congruent parallelograms. Both patterns have been used frequently in origami engineering [6–8]. Applications of each pattern take advantage of their simplicity, adaptability and unique geometric properties. The Miura-ori pattern has been modified and applied to create curved sheets [9], sandwich fold cores [7], deployable tubes [10] and three-dimensional metamaterials [3]. The eggbox pattern has been applied to sandwich fold cores [7], tunable electromagnetic arrays [11] and acoustic materials [12].

The kinematics of the Miura-ori and eggbox patterns have been studied by assuming that facets remain rigid while folds act as perfect hinges [13], which we will also assume in this paper. It can be shown that each pattern has 1 d.f., which makes the possibility of using both concurrently in the same tessellation attractive. These two patterns have contrasting properties which differentiate them. For instance, the Miura-ori pattern is developable, meaning that it can be folded from a single planar sheet, while the eggbox is non-developable. In addition, the Miura-ori pattern has one flat-folded state besides its initial unfolded configuration, while the eggbox can be flat-folded into two orthogonal states. The Miura-ori pattern has negative in-plane Poisson's ratio, while the eggbox has positive in-plane Poisson's ratio. Conversely, the Miura-ori has positive out-of-plane Poisson's ratio while the eggbox has negative out-of-plane Poisson's ratio.

The unit cells of both the Miura-ori and eggbox patterns consist of four congruent parallelograms meeting together at degree-4 vertices, shown in figure 1*a,b*. Let γ be the smaller wedge angle of the parallelogram for each pattern. In the Miura-ori, of the four wedges that meet at the central vertex, two adjacent wedges have angle γ , while the other two wedges have angle $\pi - \gamma$. For the eggbox, all four wedges that meet at the central vertex have angle γ .

The morph pattern is a generalization of the Miura-ori and eggbox patterns, with a unit cell consisting of two pairs of congruent parallelograms meeting at a vertex, rather than four congruent parallelograms in the case of the Miura-ori and the eggbox [14]. This pattern combines some of the properties of the Miura-ori and eggbox patterns, including switching between 'Miura mode' and 'eggbox mode' and a smooth transition between negative and positive Poisson's ratio.

In this paper, we study the hybrid structure formed by stitching unit cells of Miura-ori and eggbox together. We discuss its compatibility constraints and kinematics. Next, we compare the Miura-eggbox hybrid with the morph pattern. Then, we consider extended hybrid arrays combining the Miura-ori, eggbox and morph patterns. Lastly, we explore potential applications based on hybrid patterns.

2. Geometric description of hybrid patterns

Figure 1 presents the geometry and notation of the standard Miura-ori (figure 1a), standard eggbox (figure 1b) and hybrid (figure 1c) patterns. The hybrid unit cell is formed by attaching a Miura-ori unit cell and an eggbox unit cell together at two edges as shown in figure 1c. The unit cells of the Miura-ori and eggbox are each fully defined by three parameters: two edge lengths a and b , and the angle between the edges γ .

(a) Compatibility constraints

For geometric compatibility, to connect Miura-ori and eggbox unit cells, we require that

$$a_m = a_e = a \quad (2.1)$$

for each unit cell.

In addition, let us define the angle ψ as the angle between the $+y$ -direction and the fold line shared by the unit cells, as shown in figure 1. The range of ψ for the Miura-ori cell is $[0, \gamma_m]$, while the range for the eggbox cell is $[\pi/2 - \gamma_e, \pi/2]$. Therefore the range of ψ for the hybrid structure is the intersection, $[\pi/2 - \gamma_e, \gamma_m]$ (γ_m and γ_e are assumed to be acute), which results in an inequality constraint

$$\frac{\pi}{2} - \gamma_e < \gamma_m. \quad (2.2)$$

The Miura-ori and eggbox unit cells are each determined by three parameters ((a_m, b_m, γ_m) and (a_e, b_e, γ_e) , respectively). When combined to form the hybrid unit cell, the constraints reduce the number of free parameters. The hybrid unit cell is fully determined by three lengths (a, b_m, b_e) and two angles (γ_m, γ_e), where the angles must follow inequality (2.2).

(b) Locking

Let S_m and S_e be defined as half the length in the x -direction of the Miura-ori and eggbox unit cells, respectively. Parametrized as a function of ψ , the expressions for S_m and S_e are given by

$$S_m = b_m \frac{\sqrt{\sin^2 \gamma_m - \sin^2 \psi}}{\cos \psi} \quad (2.3)$$

and

$$S_e = b_e \frac{\sqrt{\sin^2 \psi - \cos^2 \gamma_e}}{\sin \psi}. \quad (2.4)$$

As ψ increases from $\pi/2 - \gamma_e$ to γ_m , S_m decreases from S_m^{\max} to 0 while S_e increases from 0 to S_e^{\max} , where S_m^{\max} and S_e^{\max} are the maximum compatible lengths of each respective unit cell given by

$$S_m^{\max} = b_m \frac{\sqrt{\sin^2 \gamma_m - \cos^2 \gamma_e}}{\sin \gamma_e} \quad (2.5)$$

and

$$S_e^{\max} = b_e \frac{\sqrt{\sin^2 \gamma_m - \cos^2 \gamma_e}}{\sin \gamma_m}. \quad (2.6)$$

Next, let us define S_h to be half the length of the hybrid unit cell in the x -direction (figure 1):

$$S_h = S_m + S_e. \quad (2.7)$$

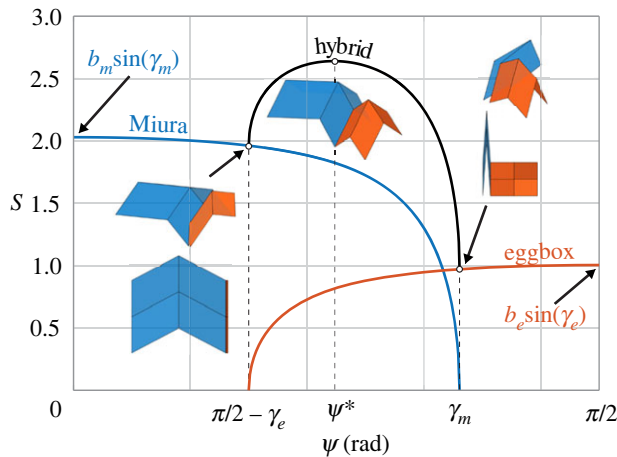


Figure 2. Plot of Miura-ori, eggbox and hybrid unit cell lengths in the x -direction against angle ψ . By definition, ψ^* is the angle for which the length of the hybrid unit cell is maximized.

As ψ increases, along the x -direction, the Miura-ori unit cell compresses while the eggbox unit cell expands. Owing to the discrepancy of the relative rates of compression and expansion, the length S_h is a non-monotonic function of the angle ψ , as shown in figure 2. This monotonic property results in a topological locking behaviour in compression. Namely, when subject to compression in the x -direction, the hybrid unit cell will actuate until the angle ψ reaches either its minimum or maximum bound and the eggbox or Miura-ori unit cell becomes flat-folded, respectively. Which unit cell becomes flat-folded is dependent on the initial state of the hybrid unit cell. Let ψ^* be the critical angle that results in the maximum value of S_h . If initially $\psi < \psi^*$, compressing the structure along the x -direction (decreasing S_h) will decrease ψ until the eggbox cell becomes flat-folded. If initially $\psi > \psi^*$, compressing the structure will increase ψ until the Miura-ori cell becomes flat-folded.

In the y -direction, half the length of the hybrid unit cell L_h is equal to that of Miura-ori and eggbox unit cells, which decreases monotonically as a function of ψ . The expression of L_h is

$$L_h = L = a \cos \psi. \quad (2.8)$$

(c) Poisson's ratio derivation

Poisson's ratio is a measure of how a material expands or contracts in the direction perpendicular to the loading direction. Following the example of Schenk [13], we choose to use the tangential Poisson's ratio [15], where the planar Poisson's ratio is the negative ratio between instantaneous strains in orthogonal directions. These are defined as

$$\varepsilon_S^h = \frac{dS_h}{S_h} \quad \text{and} \quad \varepsilon_L^h = \frac{dL}{L} \quad (2.9)$$

and

$$v_{LS}^h \equiv -\frac{\varepsilon_S^h}{\varepsilon_L^h} = \frac{S_m}{S_h} v_{LS}^m + \frac{S_e}{S_h} v_{LS}^e, \quad (2.10)$$

where ε_S^h and ε_L^h are the instantaneous strains in the x - and y -directions, respectively. v_{LS}^m and v_{LS}^e are Poisson's ratio of the Miura-ori and eggbox cells, respectively, for strains applied in the y -direction. v_{LS}^h , Poisson's ratio of the hybrid pattern, is a weighted average of those of the Miura-ori and eggbox cells, with weights proportional to the length of each unit cell in the x -direction (see appendix A). It can also be shown that the expressions for the Miura-ori and eggbox Poisson's

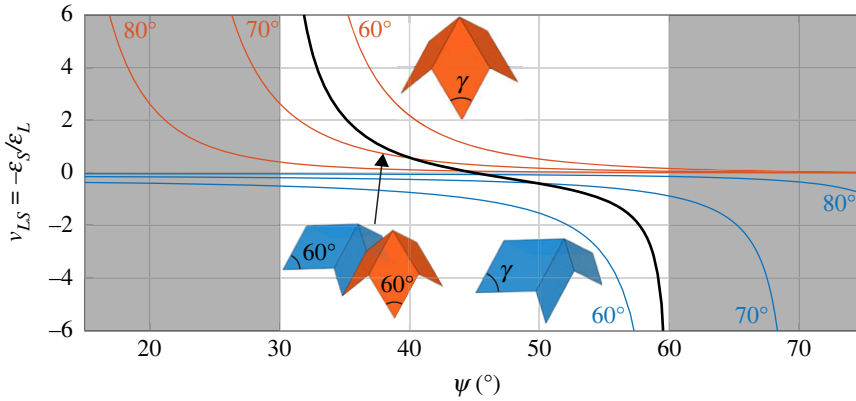


Figure 3. Poisson's ratio versus ψ for Miura-ori and eggbox unit cells with γ angles of 60° , 70° and 80° , as well as a hybrid unit cell with $\gamma_m = \gamma_e = 60^\circ$ and $b_m = b_e$ (in black). Hybrid arrays can be formed by combining instances of Miura-ori and eggbox unit cells, with Poisson's ratio of the array being a weighted average of Poisson's ratio of the constituent cells. The shaded region is unreachable for a hybrid array with minimum Miura-ori and eggbox wedge angles of 60° .

ratios are (see [13] and appendix A)

$$v_{LS}^m = -\frac{\cos^2 \gamma_m}{\sin^2 \gamma_m - \sin^2 \psi} \quad (2.11)$$

and

$$v_{LS}^e = \frac{\cos^2 \gamma_e \cot^2 \psi}{\sin^2 \psi - \cos^2 \gamma_e}. \quad (2.12)$$

Note that Poisson's ratios and lengths S in the x -direction of the Miura-ori and eggbox cells are all functions of the actuation angle ψ .

Poisson's ratio of the Miura-ori is negative and decreases without bound as ψ increases to γ_m . Poisson's ratio of the eggbox is positive and increases without bound as ψ decreases to $\pi/2 - \gamma_e$. Poisson's ratio function for various wedge angles are plotted in figure 3. As a weighted average between the two, Poisson's ratio of the hybrid unit cell decreases from positive infinity to negative infinity as ψ increases from $\pi/2 - \gamma_e$ to γ_m , as seen in black in figure 3.

(d) Hybrid arrays

Owing to the compatibility constraints specified, hybrid unit cells can be tessellated in the x - and y -directions to form a planar array. Each column along the y -direction must consist of the same type of unit cell. By contrast, in the x -direction, we are not limited to tessellations of alternating Miura-ori and eggbox rows. Any permutation of Miura-ori and eggbox rows is permissible given the previously stated compatibility constraints are satisfied. Rigid-foldability is maintained for the planar array due to the translational symmetry of the arrays composed of the basic unit cells.

Let S' and L' be half the length in the x - and y -directions, respectively, of the hybrid array. Suppose the array has $n \times n$ unit cells, with n_m strips of Miura-ori unit cells and n_e strips of eggbox unit cells such that $n_m + n_e = n$. Then,

$$S' = n_m S_m + n_e S_e \quad \text{and} \quad L' = nL \quad (2.13)$$

and

$$v_{L'S'} \equiv -\frac{\epsilon_{S'}}{\epsilon_{L'}} = \frac{n_m S_m}{S'} v_{LS}^m + \frac{n_e S_e}{S'} v_{LS}^e. \quad (2.14)$$

Poisson's ratio of the hybrid array is the weighted average of the Miura-ori and eggbox Poisson's ratios, with weights determined by the relative lengths in the x -direction for the Miura-ori and eggbox strips.

In addition, hybrid arrays are not limited to one set of Miura-ori and eggbox unit cells. In fact, freeform arrays of different geometric configurations of Miura-ori and eggbox unit cells can be combined in a single array provided a modified statement of the compatibility constraints is followed. Namely, every unit cell must have the identical a crease length. In addition, ψ_{\min} is determined by the flat-folded state of the eggbox unit cell with the smallest γ_e wedge angle, while ψ_{\max} is determined by the flat-folded state of the Miura-ori unit cell with the smallest wedge angle γ_m .

Let γ_m^i and γ_e^j be the wedge angle of the i th Miura-ori cell and j th eggbox unit cell, respectively. We define the sets of wedge angles as follows:

$$\Gamma_m = \{\gamma_m^i \mid 1 \leq i \leq n_m\} \quad \text{and} \quad \Gamma_e = \{\gamma_e^j \mid 1 \leq j \leq n_e\}. \quad (2.15)$$

Then $\psi \in [\pi/2 - \min\{\Gamma_e\}, \min\{\Gamma_m\}]$. Therefore, we require $\pi/2 - \min\{\Gamma_e\} < \min\{\Gamma_m\}$.

Satisfying these modified constraints allows the freedom to develop functionally graded arrays in which the parameters of the unit cells are varied spatially for tailored mechanical properties. Similar functionally graded origami structures have been developed based on the Miura-ori pattern [16]. When these structures are subject to compression, folding initially occurs at creases, until a portion of the structure flat-folds. Upon this self-locking, further compression requires deformation in the panels, resulting in large specific energy absorption relative to non-graded structures. Functionally graded hybrid arrays can similarly exhibit such self-locking behaviour. In addition, hybrid arrays can self-lock at two different configurations (either Miura-ori or eggbox locked, see figure 1c), which is not seen in structures consisting of Miura-ori alone.

To find Poisson's ratio of freeform arrays, we again consider an $n \times n$ array, with S_i and v_{LSi} as the lengths and Poisson's ratio of the unit cell in the i th strip. Then,

$$S' = \sum_{i=1}^n S_i \quad \text{and} \quad L' = nL \quad (2.16)$$

and

$$v_{L'S'} \equiv -\frac{\varepsilon_{S'}}{\varepsilon_{L'}} = \sum_{i=1}^n \frac{S_i}{S'} v_{LSi}. \quad (2.17)$$

Poisson's ratio of the array is again a weighted average, now of Poisson's ratio of each constituent strip of unit cells. Therefore, one has the flexibility to specify Poisson's ratio curve of the array by both choosing the set of constituent unit cell Poisson's ratio curves, as well as selecting the weights by specifying the number of strips of each unit cell. In figure 3, the Miura-ori and eggbox cells with γ angles 70° and 80° are compatible with a hybrid array with $\min\{\Gamma_e\} = \min\{\Gamma_m\} = 60^\circ$, so any Poisson's ratio function that is a weighted average of the red and blue curves could be achieved for a hybrid array. Because the range of feasible ψ angles is determined by the minimum γ angles, any such array will have $30^\circ \leq \psi \leq 60^\circ$ as shown by the non-shaded region in figure 3.

However, note that as a function of ψ , Poisson's ratio for both the Miura-ori and eggbox cells has negative slope. In addition, for a given $\min\{\Gamma_m\}$ and $\min\{\Gamma_e\}$, all the other compatible Poisson's ratio curves will fall within their range. Therefore any weighted average of compatible Poisson's ratio curves will always have negative slope and be within the limits of the Poisson's ratio function of the Miura-ori cell with minimum γ_m and the eggbox cell with minimum γ_e , which limits the feasible Poisson's ratio functions of the hybrid array.

3. Morph and hybrid patterns

The morph pattern is a generalization of the Miura-ori and eggbox patterns, with similar Poisson's ratio and locking properties as the Miura-eggbox hybrid. In this section, we will first provide an overview of the morph pattern, then compare and contrast between the morph and the Miura-eggbox hybrid pattern, and finally explore hybrid arrays incorporating Miura-ori, eggbox and morph cells.

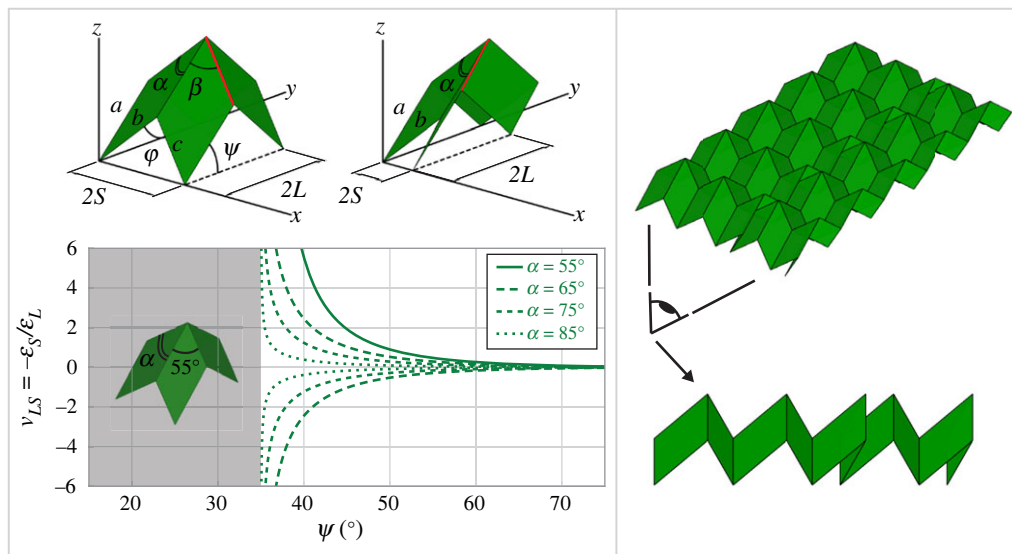


Figure 4. Geometric configuration of the morph pattern. The unit cell of the morph pattern can transition from eggbox mode (top left) to Miura mode (top centre) by switching the mountain/valley assignment of the crease highlighted in red. Poisson's ratio versus ψ for four morph unit cells with $\beta = 55^\circ$ and various values of α is shown on the bottom left. For unit cells with $\beta = 55^\circ$, the kinematic bifurcation occurs when $\psi = 35^\circ$, where Poisson's ratio transitions between positive infinity and negative infinity. The shaded region is unreachable for a morph cell with $\beta = 55^\circ$. The morph array (right) shows three rows in eggbox mode and two rows in Miura mode.

(a) Morph overview

The morph pattern is a generalization of the Miura-ori and eggbox, with a unit cell consisting of two pairs of congruent parallelograms meeting at a degree-4 vertex [14]. A unit cell of the morph pattern is shown in figure 4.¹ Two adjacent parallelograms have a wedge angle α , while the other two have a wedge angle β such that $\alpha \geq \beta$. The morph pattern allows the crease between the two β angle panels to change between mountain and valley assignments to switch between an eggbox and a Miura mode. This leads to similar properties seen in the hybrid pattern, such as a transition from positive to negative Poisson's ratio and mode locking in arrays.

Each morph unit cell has two possible modes for a given value of ψ . One expresses a positive Poisson's ratio (eggbox mode) and the other expresses a negative Poisson's ratio (Miura mode).

The morph pattern can be tessellated, for instance, to create an $n \times n$ array of unit cells, as shown in figure 4. When tessellated, Poisson's ratio of the morph array, similar to the hybrid pattern, is the weighted average of Poisson's ratio of the cells in Miura and eggbox modes.

(b) Comparing morph and hybrid patterns

The Miura-eggbox hybrid patterns consists of multiple Miura-ori and eggbox unit cells, each consisting of four parallelograms. The morph pattern consists of a single repeated unit cell which consists of four parallelograms.

The hybrid pattern's Poisson's ratio is a weighted average of Poisson's ratio of its constituent Miura-ori and eggbox unit cells. Poisson's ratios of the constituent cells are a function of their γ angles. The weights are dependent on the lengths of each unit cell and the proportion of the array each unit cell comprises. In contrast, the morph pattern's Poisson's ratio is a weighted average of the Poisson's ratio of its unit cell's Miura and eggbox modes. Poisson's ratios of the modes are a

¹The labelling scheme shown differs from that used in [14], where we have replaced a with b , b with c , c with a , and ψ with $\pi - 2\psi$.

function of the unit cell angle and length dimensions. The weights are dependent on the lengths of the cells and fraction of the cells in each mode.

Both the hybrid and morph arrays' Poisson's ratio can be controlled through a variety of parameters. The hybrid array's Poisson's ratio can be controlled by adjusting Poisson's ratio of its constituent Miura-ori and eggbox unit cells by adjusting the angle parameter of the unit cells. In addition, the fraction of Miura-ori and eggbox strips and their respective lengths can be adjusted to make the weighted average Poisson's ratio skew towards the Miura-ori or eggbox Poisson's ratio curves.

Poisson's ratio of the morph pattern can similarly be controlled by adjusting the lengths and angle parameters of the unit cell dimensions. However, unlike the hybrid array, after the geometric configuration is set, the number of strips of the morph array in Miura or eggbox modes can be changed via a kinematic bifurcation point, adjusting the weights for Poisson's ratio calculation and effectively tuning Poisson's ratio of the array. No such bifurcation exists in the hybrid array, so Poisson's ratio function is fixed for a given geometric parametrization.

Morph arrays are capable of exhibiting mode locking under either compression and tension, where unit cells will be taken away from their kinematic bifurcation point based on the local and global Poisson's ratio. Compressive mode locking occurs if Poisson's ratio is globally negative, while tensile mode locking occurs if Poisson's ratio is globally positive. For instance, in figure 5, the morph array has a globally negative Poisson's ratio. Upon x compression, the central eggbox mode unit cell expands despite the global contraction. The cell moves away from the kinematic bifurcation, preventing a transition to Miura mode. The mode locking is topological, in that the mountain and valley assignments are locked, but the pattern can still fold to flat-folded states [14]. This is in contrast to motion locking, where contact between panels prevents the pattern from reaching a flat-folded state [17]. The compressive locking in the hybrid pattern is both topological and contact based; the direction of actuation (which unit cell will flat fold) is based on the initial configuration, and the end state is limited by panels contacting when one of the constituent unit cells has flat folded. In figure 5, when compression is applied to the hybrid array, which unit cell compresses and flat folds is determined by its initial folded configuration. A summary of the comparisons between the Miura-eggbox hybrid arrays and morph arrays is outlined in table 1.

(c) Miura-eggbox-morph hybrid arrays

The morph pattern can also be incorporated to arrays of the hybrid pattern, as shown in figure 6. To join columns of different origami patterns in a compatible way, we require the interface between columns to be vertical, i.e. lie in a plane normal to the x -axis. This is guaranteed by the orthorhombic nature of the Miura-ori, eggbox and morph [14] unit cells. Each morph unit cell is oriented so that the crease that can switch mountain and valley assignment is parallel to the xz plane. In addition, we require that that crease cannot attach to a Miura-ori strip to prevent self-intersection when the morph pattern is in Miura mode. Note that the orthogonal orientation of the morph, achieved by rotating the unit by 90° about the z -direction, is not allowed, due to a lack of symmetry.

Let us define the angle ψ for the morph pattern similarly to how we defined ψ for the hybrid pattern unit cells, as shown in figure 4. For the morph, $\psi \in [\pi/2 - \beta, \pi/2]$. Therefore, for each morph unit cell incorporated to the array, $\beta > \pi/2 - \min\{\Gamma_m\}$. This compatibility constraint must be satisfied, as well as requiring the crease lengths parallel to the yz plane to have length a .

Within the stated constraints, the interface between columns of Miura-ori, eggbox, and morph unit cells behaves identically to that of two columns of Miura-ori unit cells in a conventional Miura-ori array, that of two columns of eggbox unit cells in a conventional eggbox array, or that of two columns of morph unit cells in a morph array. Therefore, the kinematics and rigid-foldability are maintained for each column.

The incorporation of strips of morph unit cells can introduce tunability to Poisson's ratio of the array. However, the transition point for the morph pattern occurs when $\psi = \pi/2 - \beta$, which is only reachable if $\beta < \min\{\Gamma_e\}$. Then, the minimum bound of ψ for the array will be $\pi/2 - \min\{B\}$,

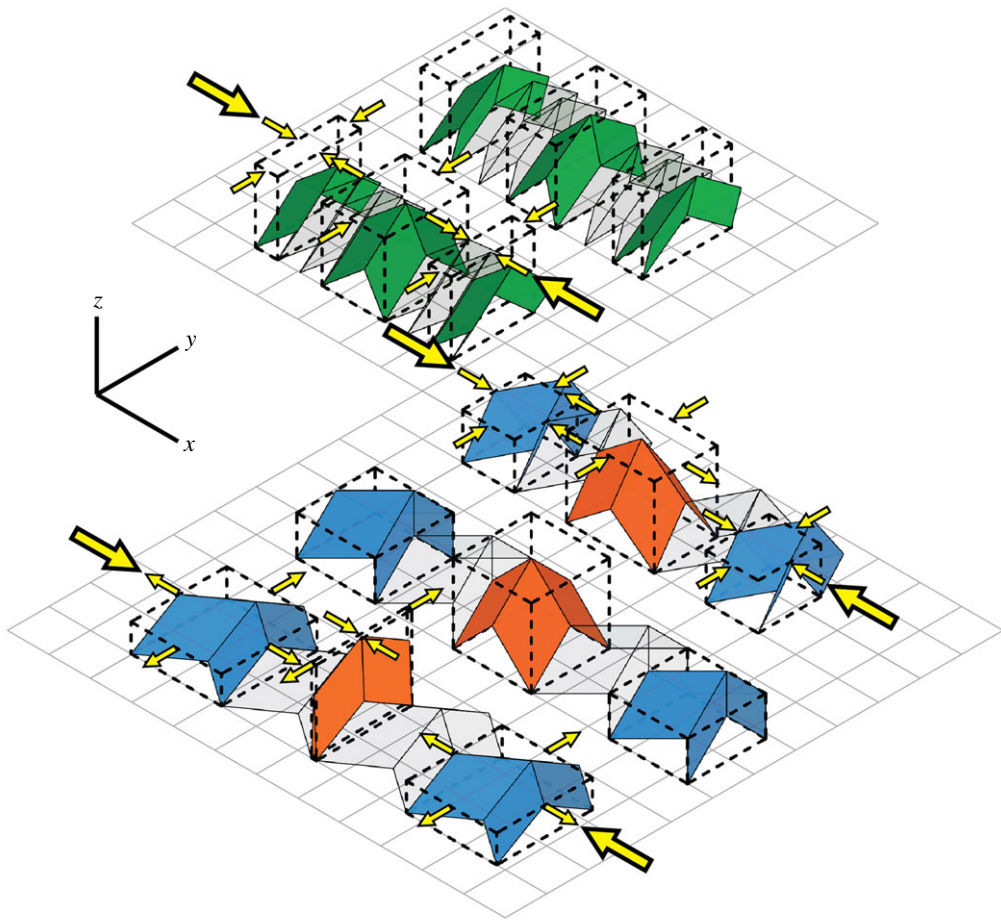


Figure 5. Comparison of locking in morph arrays and Miura-eggbox arrays. On the top, the morph array has a positive global Poisson's ratio, implying compression in the y -direction given compression in the x -direction. The central unit cell in eggbox mode is taken away from its kinematic bifurcation and grows in the x -direction despite the array globally shrinking in the x -direction. The cell is locked because it cannot smoothly transition to Miura mode. On the bottom, the Miura-eggbox array may have a positive (bottom) or negative (top) global Poisson's ratio depending on the folded configuration (value of ψ). Upon x compression, the central eggbox unit cell will shrink if $\psi < \psi^*$ (bottom) and grow if $\psi > \psi^*$ (top). Unlike for the morph, the Miura-eggbox hybrid has no kinematic bifurcation, but upon x compression ψ will always move away from the critical angle ψ^* .

where B is the set of β angles. In addition, for any morph unit cell with $\beta > \min\{B\}$, the transition ψ will not be reachable. Therefore, only morph unit cells with the minimum β angle will be able to exhibit mode switching. Figure 4 shows Poisson's ratio curves for morph patterns with $\beta = 55^\circ$ while varying α .

Let ϕ be the angle formed by the creases with length b and c . If morph unit cells follow the constraints for tunability, for a given value of ψ , the morph unit cells can have two different values of ϕ depending on if they are in Miura mode or eggbox mode. As ψ increases from $\pi/2 - \beta$ to $\pi/2$, in Miura mode, the Poisson's ratio increases from $-\infty$ and approaches 0, while in eggbox mode, Poisson's ratio decreases from $+\infty$ and approaches 0. In figure 4, note that if β is kept constant for different morph unit cells in a single array, each morph unit cell can maintain tunability.

Poisson's ratio of an array with strips of Miura, eggbox and morph unit cells is once again the weighted average of Poisson's ratio of its constituent unit cells, with weights determined by

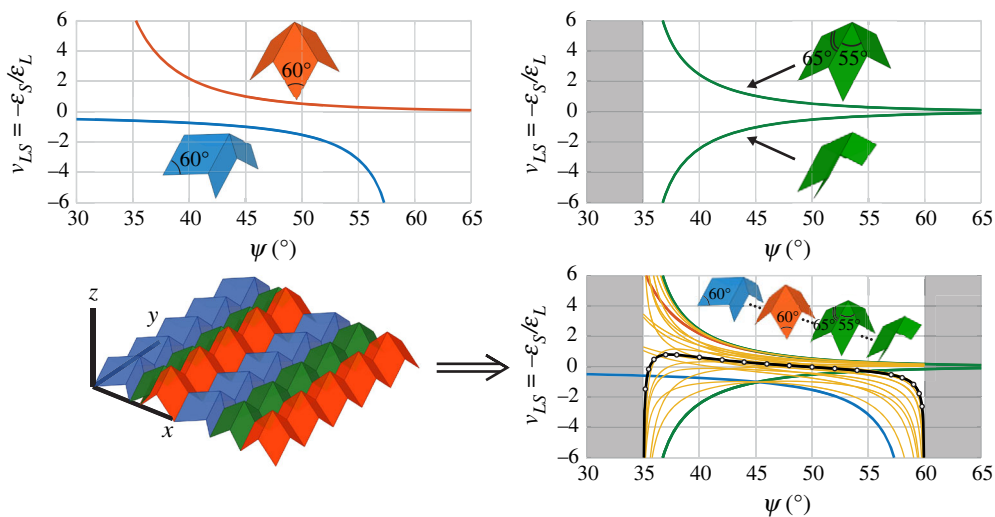


Figure 6. Poisson's ratio of a hybrid array is a weighted average of Poisson's ratios of its constituent cells. Miura-ori unit cells with $\gamma_m = 60^\circ$ (top left), eggbox unit cells with $\gamma_e = 60^\circ$ (top left) and morph unit cells with $\alpha = 65^\circ$ and $\beta = 55^\circ$ (top right) can combine to form hybrid arrays (bottom left) with Poisson's ratios that span Poisson's ratio bounds of its constituent cells (bottom right). Each curve in yellow is Poisson's ratio function for a given combination of Miura-ori, eggbox and morph cells using different weights. In black, one combination is highlighted which exhibits a Poisson's ratio that transitions from negative to positive back to negative values, overlaid with results from numerical simulations using MERLIN software (circular markers). The highlighted Poisson's ratio can be achieved using a combination of 1 Miura-ori unit cell, 2 eggbox cells, 3 morph cells in Miura mode and 1 morph cell in eggbox mode assuming unit cells with $b_m = b_e = c_{\text{mor}}$, where c_{mor} is the length of the crease on the morph cell denoted by c in figure 4. Note that the weighting depends only on the total proportion of the x length occupied by each constituent unit cell, so an equivalent Poisson's ratio can be achieved by scaling the b_m , b_e and c_{mor} parameters and inversely scaling the number of each respective unit cell in the array.

Table 1. Comparison between Miura-eggbox hybrid arrays and morph arrays.

	Miura-eggbox hybrid array	morph array
composition	multiple different Miura-ori and eggbox unit cells	single identical morph unit cell
Poisson's ratio	weighted average of that of the constituent Miura-ori and eggbox unit cells	weighted average of that of the Miura and eggbox modes of the morph unit cell
tunability	Poisson's ratio function fixed after geometry defined	Poisson's ratio function tunable via mode transitions through a kinematic bifurcation point
locking	locking under x compression	locking under either x tension or x compression

their relative lengths in the x -direction. Therefore, with the morph cells in Miura mode, Poisson's ratio of the array can be a weighted average of Poisson's ratio functions with negative and positive slopes with respect to ψ . This allows arrays with Poisson's ratio that are non-monotonic, as shown in figure 6. This is in contrast to the Miura-eggbox hybrid arrays, which can only have negative slope. In addition, this allows mode locking in both compression and tension.

Furthermore, Poisson's ratio can transition from negative, to positive, and back to negative again. This is in contrast to the morph alone, which can have non-monotonic Poisson's ratio, but can only change in sign once.

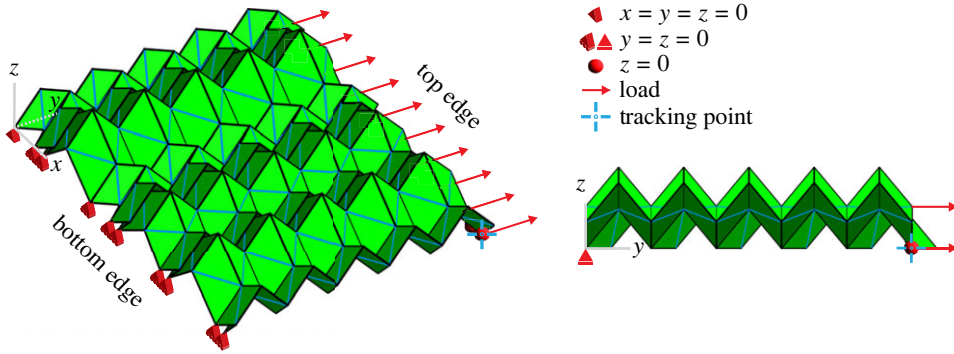


Figure 7. Specification of boundary conditions and loading of MERLIN numerical simulation of array in figure 8a (CAD and physical models) with Poisson's ratio shown in figure 6.

The theoretical Poisson's ratio function of an array displaying the non-monotonic behaviour shown in figure 6 was numerically simulated using MERLIN, a nonlinear 'bar-and-hinge' model developed for analysing quasi-static origami structures [18]. Model parameters for Young's modulus (10^9), bar area (10^{-4}) and bending (10^5) and folding (10^{-1}) stiffness were chosen to asymptotically approach rigid panels.

The boundary conditions were specified to pin the bottom left corner to the origin, constrain every other bottom vertex along the x -axis, and constrain every other top vertex to the xy -plane, as shown in figure 7. The load was applied in the $+y$ -direction at each top vertex. The boundary conditions were chosen to resemble an experimental set-up using the Saint-Venant Fixture described in [19] to experimentally verify Poisson's ratio of origami metamaterials. Poisson's ratio was calculated by tracking the position and displacement of the top right vertex highlighted in blue in figure 7. The angle ψ was calculated using the edge connected to the origin. The results of the numerical simulations are overlaid in figure 6 using circular markers and show excellent agreement with the theoretical curve.

4. Potential applications

Hybrid patterns can combine geometrical properties such as Poisson's ratio and tunability of their constituent patterns, as well as display new behaviours. This can be an avenue for applications from materials scale metamaterials to architectural scale deployable structures which take advantage of tunable Poisson's ratio, locking configurations and complex shape changing. We discuss three such potential applications.

(a) Planar arrays

The hybrid pattern can be used to create planar arrays with specified physical properties and kinematics. For instance, one could create facades with specified motions, or develop arrays that exhibit Poisson's ratio ranging from positive to negative infinity. One could also design a metamaterial with near zero Poisson's ratio for a large range of lengths.

With the addition of the morph pattern to the array, the envelope of possible Poisson's ratios is bounded by the minimum of the Miura-ori and morph in Miura mode unit cells from the bottom, and the eggbox and morph in eggbox unit cells from the top, as shown in figure 6. One could design arrays with Poisson's ratios that transition from the negative to positive and back to negative, as shown in figure 8a. In addition, the morph pattern allows additional tunability via the kinematic bifurcation point, allowing certain rows of the morph to switch between Miura and eggbox mode after the geometric configuration is set.

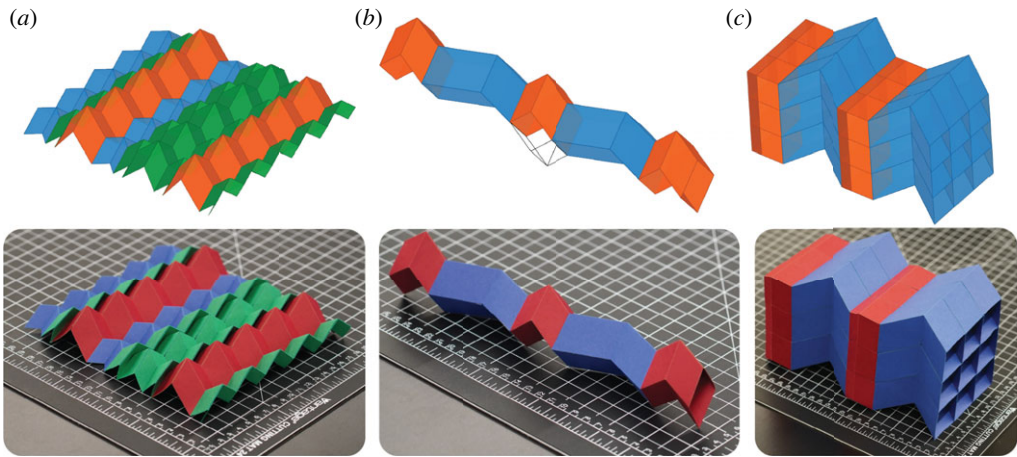


Figure 8. CAD and physical models of potential applications. (a) Hybrid array with the non-monotonic Poisson's ratio curve shown in figure 6. The array has five rows and nine columns, which from left to right are (i) Miura, (ii) morph (Miura mode), (iii) eggbox, (iv) Miura, (v) morph (Miura mode), (vi) morph (eggbox mode), (vii) morph (Miura mode), (viii) eggbox and (ix) morph (Miura mode). Note the consistency of this model and the MERLIN computer model of figure 7. (b) Tube made from reflecting a hybrid unit cell about the xy plane. Note that the kinematics of the hybrid tube is identical to a tube where the eggbox section is replaced with a corresponding rotated Miura tube section, which is created by replacing the eggbox unit cell below the xy plane (black wireframe) with four congruent parallelograms which convert the section to a rotated Miura tube section. (c) Metamaterial formed from rotated Miura tubes.

The arrays can also be designed as metamaterials with specified end configurations. For instance, one can design a hybrid array with end configurations that differ in length by a factor of two. Under compression, such an array would have very low stiffness until one of the two specified end configurations is reached, at which point the stiffness would increase sharply. There are infinitely many arrays that can achieve this behaviour, for instance an array of alternating columns of Miura-ori and eggbox cells with $\gamma_m = \gamma_e = 60^\circ$ and $b_m = 2b_e$.

(b) Tubes

Taking inspiration from Miura tubes formed by mirroring a single row of the Miura-ori pattern [10], we form a hybrid tube by reflecting a row of Miura-ori and eggbox unit cells, which will maintain the locking behaviour seen in the planar patterns. Rigid-foldability is maintained, as the kinematics of the reflected cells matches those of the original pattern. The sections of the tube corresponding to eggbox cells will have holes; however, from observing the geometry of the hybrid tube in figure 8*b*, it is clear that the kinematics matches those of a tube with eggbox tube sections replaced with Miura-ori tube sections rotated 90° about the long axis. To complete this transformation, the original eggbox panels above the xy plane remain unaltered, while the eggbox panels below the xy plane are translated to complete the Miura-ori tube section. This provides a method to create a tube with the same kinematic properties without requiring holes in the tube.

We will show the rigid-foldability of these rotated Miura tubes. Each Miura-ori tube section is rigid-foldable with 1 d.f. [10]. All that remains to be shown is that adjacent Miura-ori tube sections that are rotated 90° relative to each other remain geometrically compatible and rigid-foldable when combined. The interface between adjacent tube sections consists of a rhombus with side length a . Both Miura-ori tube sections are able to rigidly fold to match any such rhombus. This allows adjacent sections to be attached compatibly and act as a rigid-foldable assembly.

Unlike conventional Miura tubes, the hybrid or rotated Miura tubes are capable of supporting a compressive load, due to the increased stiffness from motion locking. This increased stiffness

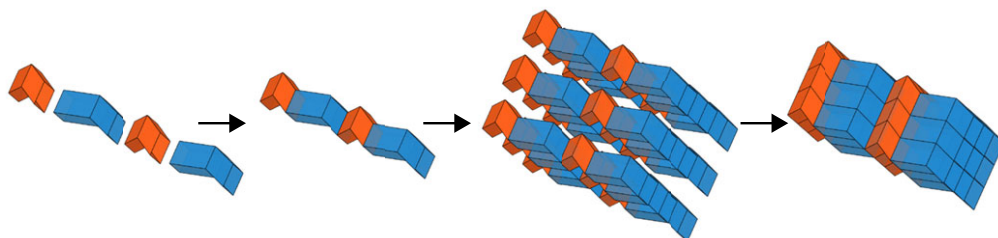


Figure 9. Conceptual metamaterial construction process by tessellating rotated Miura tubes. This process illustrates how figure 8c was obtained.

comes with the cost of losing flat-foldability. Also, in contrast to similar Miura-ori inspired tube and metamaterial structures that experience increased stiffness due to motion locking when a single set of facets come into contact [20,21], the hybrid tubes can exhibit motion locking from two separate sets of contacting faces which can be selected based on the initial configuration when compression is applied. Thus, the hybrid tubes allow a degree of tunability after the geometric configuration is set.

As shown in figure 2, the length of the hybrid pattern at the limits of its actuation range are determined by the length of the Miura-ori and eggbox unit cells. Therefore, one can design a tube that has a large expansion ratio between its deployed and stowed length. Alternatively, one could design for a specific ratio between its deployed and stowed length, for instance to make a tube that will exactly double in size, similar to the planar case.

Note that the technique used to remove holes from the tube corresponding to eggbox cells cannot be fully replicated for morph cells, because as the morph tube section transitions from eggbox mode to Miura mode via the kinematic bifurcation point, the panels self-intersect, preventing the Miura mode from being reached. As a result, we have not shown the morph pattern included in tubes or the subsequent section on metamaterials.

(c) Three-dimensional metamaterials

Extending the pattern to three dimensions, the rotated Miura tube discussed previously can be tessellated to form a three-dimensional metamaterial with configurable Poisson's ratio and locking behaviour, as shown in figure 8c. To construct the metamaterial, rotated Miura tubes are tessellated in two dimensions via repetitive translation along two principal axes. Both principal axes are orthogonal to the long axis of the tube. Each of the principal axes are parallel to one pair of sides of the interfacial rhombus discussed previously. This process is illustrated in figure 9. The metamaterial maintains rigid-foldability due to the two-dimensional translational symmetry of its construction. This structure could be applied as an architected material with a large degree of tunability. Properties such as mechanical anisotropy, high strength-to-density ratios and shape recoverability could be achieved through the design of panel and crease stiffnesses. Additionally, such three-dimensional metamaterials will exhibit high specific energy absorption similar to the functionally graded origami structures demonstrated in [16]. This is because the hybrid pattern inherently exhibits self-locking, even without functional grading. Further control of the force displacement curve can be achieved by functionally grading the hybrid pattern, resulting in additional increases of stiffness as more instances of self-locking are introduced.

The ability to design different locked states enables architected materials that can sharply increase in stiffness at two specified deformed states. In addition, reversible auxeticity can be achieved where Poisson's ratio switches sign during deformation. Such origami inspired metamaterials are geometrically scalable and have been demonstrated at micron length scales [3].

To demonstrate the concept of a three-dimensional metamaterial with different locking states, we numerically simulate the structure shown in figure 8c in compression using MERLIN. The

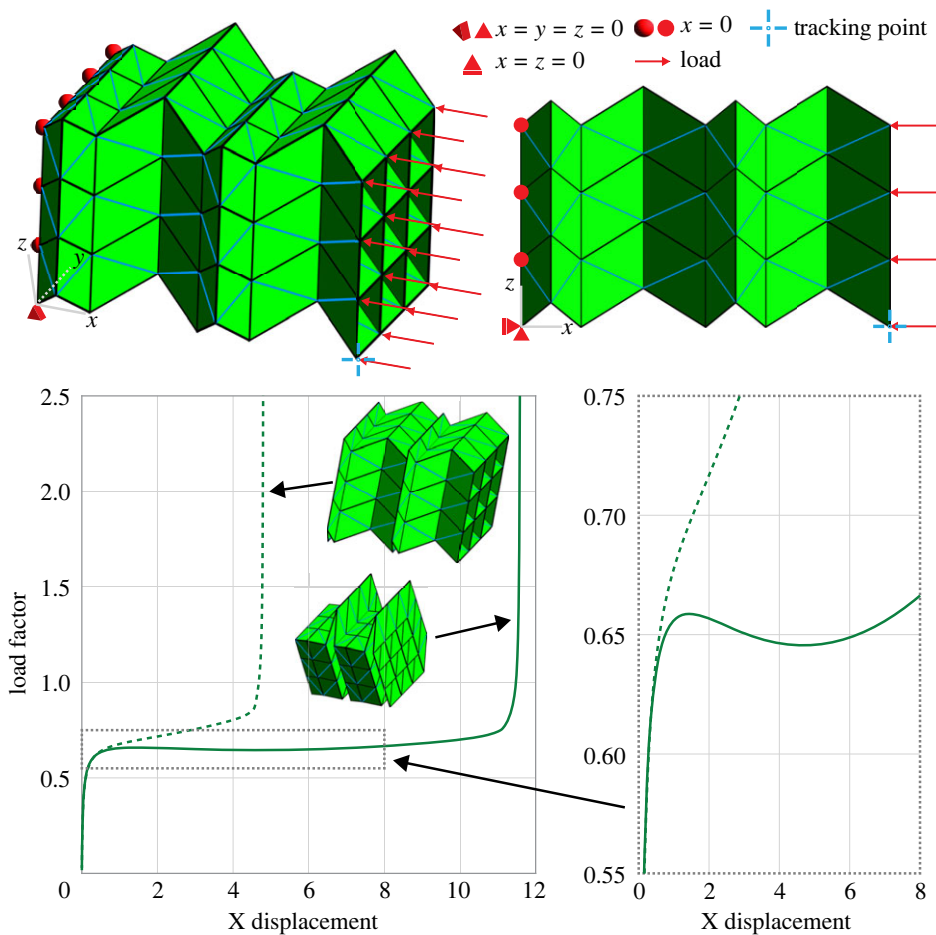


Figure 10. Specification of boundary conditions and loading for MERLIN numerical simulation of the three-dimensional metamaterial in figure 8c and load versus displacement plot for two initial configurations (in the neighbourhood of the ψ^* point of figure 2). The zoomed in plot on the bottom right highlights a softening behaviour along one branch of the load displacement curve.

material parameters match those used previously for the hybrid array. The boundary conditions were specified such that the bottom left vertex was pinned at the origin, the vertices on the left face were constrained to the yz -plane, and the vertices on the bottom left edge were constrained to the y -axis, as shown in figure 10. Two simulations were conducted in the neighbourhood of the ψ^* point of figure 2. One in which initially $\psi > \psi^*$, causing the second and fourth layer of cells to flat fold, and another in which initially $\psi < \psi^*$, causing the first and third layer of cells to flat fold. In the numerical model, the constitutive model of folding hinges is nonlinear and approaches infinite stiffness when the dihedral angle approaches zero to prevent panel intersection. The force versus displacement demonstrates conceptually how stiffness increases dramatically when the locked configurations are reached, and how two different end states can be reached depending on the initial configuration.

5. Concluding remarks

In this paper, we introduced and analysed the geometric mechanics of an origami pattern combining Miura-ori, eggbox and morph unit cells. We first derive the compatibility requirements to form the hybrid structure, then analyse the geometric properties that result from the kinematic

coupling of the constituent patterns. The resultant arrays can demonstrate mode locking, Poisson's ratios that range from negative infinity to positive infinity, and non-monotonic Poisson's ratios.

The hybrid pattern can be used in a variety of potential applications, including arrays, tubes, and three-dimensional metamaterials. In addition, the pattern can be used to develop functionally graded metamaterials with self-locking properties and high specific energy absorption.

Future work could verify the in-plane Poisson's ratio experimentally in a similar manner to [19] and compare with theoretical and numerical results. Poisson's ratio in bending could also be analytically determined as has been done with the Miura-ori [22], eggbox [23], morph [14] and other tessellated patterns [24,25].

Hybrid patterns provide the ability to not only combine properties such as Poisson's ratio and tunability of their components, but also derive mechanical properties beyond their constituent patterns such as self-locking and non-monotonic Poisson's ratio. We anticipate that this added functionality and design freedom will allow hybrid patterns to be used in various engineering applications requiring programmable and reconfigurable structures.

Data accessibility. The data are provided in electronic supplementary material [26].

Declaration of AI use. We have not used AI-assisted technologies in creating this article.

Authors' contributions. K.T.L.: conceptualization, data curation, formal analysis, investigation, methodology, software, validation, visualization, writing—original draft, writing—review and editing; G.H.P.: conceptualization, investigation, resources, supervision, validation, visualization, writing—review and editing.

All authors gave final approval for publication and agreed to be held accountable for the work performed therein.

Conflict of interest declaration. We declare we have no competing interests.

Funding. K.T.L. and G.H.P. acknowledge support from the Margareta Engman Augustine Professorship of Engineering at Princeton University.

Acknowledgements. The authors thank Prof. Tomohiro Tachi for his suggestion of rotated Miura tubes, Dr Xiangxin Dang for his helpful suggestions in editing the paper, and Hannah Kim for her graphical assistance.

Appendix A. Derivation of hybrid Poisson's ratio

(a) Miura-ori and eggbox

Using the notation of figure 1 and the angle θ from [6], we obtain the following relationships for the Miura-ori cell:

$$\theta = \sin^{-1} \left(\frac{\sin \psi}{\sin \gamma_m} \right) \quad (\text{A } 1)$$

and

$$\cos \theta = \frac{\sqrt{\sin^2 \gamma_m - \sin^2 \psi}}{\sin \gamma_m}. \quad (\text{A } 2)$$

Schenk derived Poisson's ratio in terms of θ [6], which we will rewrite in terms of ψ :

$$\begin{aligned} \nu_{LS}^m &= -\frac{1}{\cos^2 \theta \tan^2 \gamma_m} \\ &= -\frac{\sin^2 \gamma_m}{(\sin^2 \gamma_m - \sin^2 \psi) \tan^2 \gamma_m} \\ &= -\frac{\cos^2 \gamma_m}{\sin^2 \gamma_m - \sin^2 \psi}. \end{aligned} \quad (\text{A } 3)$$

Similarly, for eggbox (figure 1), we obtain:

$$\alpha = \frac{\pi}{2} - \psi \quad (\text{A } 4)$$

and

$$\begin{aligned} v_{LS}^e &= \frac{\cos^2 \gamma_e \tan^2 \alpha}{\cos^2 \alpha - \cos^2 \gamma_e} \\ &= \frac{\cos^2 \gamma_e \cot^2 \psi}{\sin^2 \psi - \cos^2 \gamma_e}. \end{aligned} \quad (\text{A5})$$

(b) Hybrid unit cell

Using the notation established by figure 1, we obtain the following relationships for Miura-eggbox hybrid cells:

$$\begin{aligned} v_{LS}^h &\equiv -\frac{\varepsilon_S^h}{\varepsilon_L^h} \\ &= -\frac{L}{S_h} \frac{dS_h}{dL} \\ &= -\frac{L}{S_h} \frac{dS_m + dS_e}{dL} \\ &= -\left(\frac{L}{S_h} \frac{dS_m}{dL} + \frac{L}{S_h} \frac{dS_e}{dL} \right) \\ &= -\left(\frac{S_m}{S_h} \frac{L}{S_m} \frac{dS_m}{dL} + \frac{S_e}{S_h} \frac{L}{S_e} \frac{dS_e}{dL} \right) \\ &= \frac{S_m}{S_h} v_{LS}^m + \frac{S_e}{S_h} v_{LS}^e. \end{aligned} \quad (\text{A6})$$

(c) Hybrid arrays

Repeating the calculation for planar Poisson's ratio for hybrid arrays consisting of multiple Miura-ori and eggbox rows:

$$S' = n_m S_m + n_e S_e, \quad (\text{A7})$$

$$L' = nL \quad (\text{A8})$$

and

$$\begin{aligned} v_{L'S'} &\equiv -\frac{\varepsilon_{S'}}{\varepsilon_{L'}} \\ &= -\frac{L'}{S'} \frac{dS'}{dL'} \\ &= -\left(\frac{L'}{S'} \frac{n_m dS_m}{dL'} + \frac{L'}{S'} \frac{n_e dS_e}{dL'} \right) \\ &= -\left(\frac{n_m S_m}{S'} \frac{L'}{S_m} \frac{dS_m}{dL'} + \frac{n_e S_e}{S'} \frac{L'}{S_e} \frac{dS_e}{dL'} \right) \\ &= \frac{n_m S_m}{S'} v_{LS}^m + \frac{n_e S_e}{S'} v_{LS}^e. \end{aligned} \quad (\text{A9})$$

References

- Meloni M, Cai J, Zhang Q, Sang-Hoon Lee D, Li M, Ma R, Parashkevov TE, Feng J. 2021 Engineering origami: a comprehensive review of recent applications, design methods, and tools. *Adv. Sci.* **8**, 2000636. (doi:10.1002/advs.202000636)
- Miura K. 1985 Method of packaging and deployment of large membranes in space. *Inst. Space Astronaut. Sci. Rep.* **618**, 1–9.
- Lin Z, Novelino LS, Wei H, Alderete NA, Paulino GH, Espinosa HD, Krishnaswamy S. 2020 Folding at the microscale: enabling multifunctional 3D origami-architected metamaterials. *Small* **16**, 2002229. (doi:10.1002/sml.202002229)

4. Wu S, Ze Q, Dai J, Udipi N, Paulino GH, Zhao R. 2021 Stretchable origami robotic arm with omnidirectional bending and twisting. *Proc. Natl Acad. Sci. USA* **118**, e2110023118. (doi:10.1073/pnas.2110023118)
5. Fonseca LM, Rodrigues GV, Savi MA. 2022 An overview of the mechanical description of origami-inspired systems and structures. *Int. J. Mech. Sci.* **223**, 107316. (doi:10.1016/j.jimecs.2022.107316)
6. Schenk M, Guest SD. 2013 Geometry of Miura-folded metamaterials. *Proc. Natl Acad. Sci. USA* **110**, 3276–3281. (doi:10.1073/pnas.1217998110)
7. Xiang X, Lu G, You Z. 2020 Energy absorption of origami inspired structures and materials. *Thin-Walled Struct.* **157**, 107130. (doi:10.1016/j.tws.2020.107130)
8. Vasudevan SP, Pratapa PP. 2021 Origami metamaterials with near-constant Poisson functions over finite strains. *J. Eng. Mech.* **147**, 04021093. (doi:10.1061/(ASCE)EM.1943-7889.0002002)
9. Tachi T. 2009 Generalization of rigid-foldable quadrilateral-mesh origami. *J. Int. Assoc. Shell Spat. Struct.* **50**, 173–179.
10. Filipov ET, Tachi T, Paulino GH. 2015 Origami tubes assembled into stiff, yet reconfigurable structures and metamaterials. *Proc. Natl Acad. Sci. USA* **112**, 12321–12326. (doi:10.1073/pnas.1509465112)
11. Cui Y, Bahr R, Van Rijs S, Tentzeris M. 2021 A novel 4-DOF wide-range tunable frequency selective surface using an origami ‘eggbox’ structure. *Int. J. Microw. Wirel. Technol.* **13**, 727–733. (doi:10.1017/S1759078721000799)
12. Pratapa PP, Suryanarayana P, Paulino GH. 2018 Bloch wave framework for structures with nonlocal interactions: application to the design of origami acoustic metamaterials. *J. Mech. Phys. Solids* **118**, 115–132. (doi:10.1016/j.jmps.2018.05.012)
13. Schenk M. 2012 Folded shell structures. PhD thesis, University of Cambridge.
14. Pratapa PP, Liu K, Paulino GH. 2019 Geometric mechanics of origami patterns exhibiting Poisson’s ratio switch by breaking mountain and valley assignment. *Phys. Rev. Lett.* **122**, 155501. (doi:10.1103/PhysRevLett.122.155501)
15. Smith C, Wootton R, Evans K. 1999 Interpretation of experimental data for Poisson’s ratio of highly nonlinear materials. *Exp. Mech.* **39**, 356–362. (doi:10.1007/BF02329817)
16. Yuan L, Dai H, Song J, Ma J, Chen Y. 2020 The behavior of a functionally graded origami structure subjected to quasi-static compression. *Mater. Des.* **189**, 108494. (doi:10.1016/j.matdes.2020.108494)
17. Fang H, Li S, Wang K. 2016 Self-locking degree-4 vertex origami structures. *Proc. R. Soc. A* **472**, 20160682. (doi:10.1098/rspa.2016.0682)
18. Liu K, Paulino GH. 2017 Nonlinear mechanics of non-rigid origami: an efficient computational approach. *Proc. R. Soc. A* **473**, 20170348. (doi:10.1098/rspa.2017.0348)
19. Misseroni D, Pratapa PP, Liu K, Paulino GH. 2022 Experimental realization of tunable Poisson’s ratio in deployable origami metamaterials. *Extr. Mech. Lett.* **53**, 101685. (doi:10.1016/j.eml.2022.101685)
20. Fang H, Chu SCA, Xia Y, Wang KW. 2018 Programmable self-locking origami mechanical metamaterials. *Adv. Mater.* **30**, 1706311. (doi:10.1002/adma.201706311)
21. Gao J, You Z. 2022 Origami-inspired Miura-ori honeycombs with a self-locking property. *Thin-Walled Struct.* **171**, 108806. (doi:10.1016/j.tws.2021.108806)
22. Wei ZY, Guo ZV, Dudte L, Liang HY, Mahadevan L. 2013 Geometric mechanics of periodic pleated origami. *Phys. Rev. Lett.* **110**, 215501. (doi:10.1103/PhysRevLett.110.215501)
23. Nassar H, Lebée A, Monasse L. 2017 Curvature, metric and parametrization of origami tessellations: theory and application to the eggbox pattern. *Proc. R. Soc. A* **473**, 20160705. (doi:10.1098/rspa.2016.0705)
24. Liu K, Pratapa PP, Misseroni D, Tachi T, Paulino GH. 2022 Triclinic metamaterials by tristable origami with reprogrammable frustration (Adv. Mater. 43/2022). *Adv. Mater.* **34**, 2270298. (doi:10.1002/adma.202270298)
25. McInerney J, Paulino GH, Rocklin DZ. 2022 Discrete symmetries control geometric mechanics in parallelogram-based origami. *Proc. Natl Acad. Sci. USA* **119**, e2202777119. (doi:10.1073/pnas.2202777119)
26. Liu KT, Paulino GH. 2024 Geometric mechanics of hybrid origami assemblies combining developable and non-developable patterns. Figshare. (doi:10.6084/m9.figshare.c.7021226)